

Laser-driven formation of ZnSnO₃/CNT heterostructure and its critical role in boosting performance of the triboelectric nanogenerator

Kangpyo Lee^{a,b,1}, HyukSu Han^{c,1}, Jeong Ho Ryu^{d,1}, Sukhyun Kang^a, Kyunghwan Jung^a, Young-Kwang Kim^e, Taeseup Song^b, Sungwook Mhin^{f,**}, Kang Min Kim^{a,*}

^a Korea Institute of Industrial Technology, 137-41 Gwahakdanji-ro, Gangneung-si, Gangwon, 25440, Republic of Korea

^b Department of Energy Engineering, Hanyang University, Seoul, 04763, Republic of Korea

^c Department of Energy Engineering, Konkuk University, 120 Neungdong-ro, Seoul, 05029, Republic of Korea

^d Department of Materials Science and Engineering, Korea National University of Transportation, Chungju, Chungbuk, 27469, Republic of Korea

^e Virtual Lab. Inc., 38 Wangsimni-ro, Seongdong-gu, Seoul, 04799, Republic of Korea

^f Department of Advanced Materials Engineering Kyonggi University, Suwon, 16227, Republic of Korea

ARTICLE INFO

Keywords:

Formation mechanism
Polydimethylsiloxane
Carbon nanotube
Triboelectric nanogenerator
Pulse laser ablation

ABSTRACT

Triboelectric nanogenerators (TENGs) as energy harvesters have been extensively investigated due to their ability to convert mechanical energy to electricity through the effective coupling of triboelectrification and electrostatic induction. Herein, we introduce polydimethylsiloxane (PDMS)-based TENG prepared using ZnSnO₃ (ZTO) nanostructure on surface-modified carbon nanotubes (SMCs), which shows high power density suitable to different types of practical applications in energy harvesting and self-power system. TENG with 0.3 wt% ZTO-SMC exhibits an output voltage of 665.63 V and a current density of 137.08 mA m⁻², corresponding to improvements of 295% and 453%, respectively, with those of a pristine PDMS-based TENG. The peak power density of the TENG is 10.57 W m⁻² at a load resistance of 7 MΩ. The formation mechanism of ZTO on the SMCs (ZTO-SMC) and its effect on the TENG performance are demonstrated using density functional theory calculations. It is demonstrated that the enhanced output performance of the PDMS-based TENG using the ZTO-SMC is attributed to the synergetic effect of the enhanced dielectric constant, press-induced polarization, and effective frictional area in the triboelectric layer. This work gives a scientific and technical understanding of not only the formation of heterostructure through interface nanoengineering but also the development of polymer-based TENGs with enhanced triboelectric performance for use in energy harvesting and self-powered systems.

1. Introduction

Wireless and wearable electronic devices for the Internet of Things (IoT) technology have rapidly developed and is gradually integrating into our daily life [1,2]. Recent technological progress in energy harvesting systems is prospective to fully replace battery-driven wireless devices, thereby achieving self-powered devices for IoT [3–6]. Energy harvesting is eco-friendly technology to generate electricity from ubiquitous mechanical energy via triboelectric [7,8], piezoelectric [9,10], pyroelectric [11,12], and electromagnetic conversion [13,14]. Among them, triboelectric nanogenerators (TENGs) are considered promising power sources due to their high energy efficiency, reliability, and

cost-effectiveness [15–25]. It is believed that the energy conversion efficiency of the TENGs depends on the coupling of the triboelectrification with electrostatic induction, related to surface charge density and charge transportation [26–29]. Thus, it is important to achieve higher surface charge density and more effective charge transfer for improving the performance of the TENGs, and thus, a unique design strategy for the triboelectric layer is needed [30–33].

Polydimethylsiloxane (PDMS) with high electronegativity, flexibility, and biocompatibility has been widely utilized as a cathode material in TENGs, however, exhibiting low output and conversion efficiency impeding their use in practical energy harvesting systems [34]. One of the strategies to enhance the performance of the

* Corresponding author.

** Corresponding author.

E-mail addresses: swmhin@kyonggi.ac.kr (S. Mhin), kmmkim@kitech.re.kr (K.M. Kim).

¹ K. Lee, H. Han and J. H. Ryu contributed equally to this work.

PDMS-based TENGs is the incorporation of ferroelectric additives (e.g., ZnO, BaTiO₃, SrTiO₃, ZnSnO₃ (ZTO)) into the PDMS layer, which can enhance the dielectric permittivity of the triboelectric layer [35–40]. Besides, compared with dielectric fillers, carbon materials are reported to have higher dielectric constant through polarization by charges bound on the triboelectric layer [41–43]. For example, typical CNTs serve as capacitive structures to store electric energy through polarization [44]. It is reported that co-additives with ferroelectric and carbon-based materials in the triboelectric layer can be a good strategy to achieve further high output performance of the TENGs [45–48]. However, there are several limitations to applying the co-additives to the PDMS-based triboelectric layer, resulting in reduced TENG performance. For instance, an excessive number of ferroelectrics obstruct the charge transfer to reduce the TENG performance [49]. Alternately, percolation phenomena induced by cross-linking of excessive carbon-based materials can generate a current leak, reducing the surface charge density induced by triboelectricity [50,51]. Therefore, it is required to develop a unique methodology for co-filler with a homogeneous distribution of both ferroelectrics and carbon-based materials within the PDMS layer, enhancing the output performance of the TENG device. To achieve this goal, we developed pulsed laser ablation (PLA) technique for the functionalization of carbon nanotubes, surface-modified carbon nanotubes (SMCs), which act as an additive in the PDMS layer to enhance the performance of the TENGs. We suggested that the functional groups present on the SMC with optimized conditions could inhibit aggregation and/or cross-linking of CNTs, thereby improving the output performance of TENGs [52]. In addition to that, we modified the methodology to develop the unique co-additive composed of ferroelectric ZTO nano hemisphere on SMCs (ZTO-SMC) for piezoelectric nanogenerator (PENG) suitable to high-power energy harvesting [39]. It is noted that both functionalization of the carbon nanotubes and laser-assisted synthesis for the formation of nano ferroelectrics occurs during one-pot processing. We suggested that PLA is a suitable methodology to not only enhance dielectric properties but also promote dispersion of the additives within polymer-based matrices such as PDMS, and Polyvinylidene fluoride (PVDF). However, the underlying mechanism behind the formation of the effective co-additives is still lacking, and thus the origin of the enhanced output performance of the nanogenerators remains unclear.

Herein, we report the formation mechanism of the co-additives, ZTO-SMC, and the origin of the enhanced TENG output performance using combined experimental and computational methods. Density functional theory (DFT) calculation is carried out to demonstrate the formation mechanism of the ZTO-SMC, and experimental verification follows to achieve the highest TENG performance. A novel interface engineering strategy for the ZTO-SMC as effective co-additives in the PDMS-based triboelectric layer was selected to significantly enhance the output performance of TENGs. Experiments indicate that optimized ZTO-SMC TENG shows the highest output voltage (665.63 V), current (137.08 mA m⁻²), and power density (10.57 W m⁻²), which simultaneously power 488 commercial light emitting diode (LED) bulbs connected in series.

2. Experimental

2.1. Fabrication of ZTO-SMC

ZTO on surface-modified carbon nanotubes (denoted as ZTO-SMC) was prepared via the Pulsed laser ablation (PLA) process. In detail, multi-walled CNTs (0.5 g, Hanwha Chem), zinc nitrate hexahydrate (Zn(NO₃)₂·6H₂O, 2.0 g, Sigma Aldrich), and Sn(II) 2-ethylhexanoate (Sn(Oct)₂, 2.0 g, Alfa Aesar) powders were dissolved in high-purity ethanol (500 mL). Subsequently, the prepared solution was placed in a vial and ablated using a 10 Hz pulsed laser beam for 1 h (355 nm, third harmonic, and 10 ns pulse width) from a Q-switch ND:YAG laser system at room temperature and in ambient air. The laser beam was focused on a spot

with an area of ~2 mm² with an ablation energy of 100 mJ. Finally, ZTO-SMC was obtained through filtering and drying processes.

2.2. Computational details

DFT calculations were performed using the generalized gradient approximation (GGA) with Perdew–Burke–Ernzerhof (PBE) parameterization and Quantum espresso (QE) from Materials Square (Web-based DFT calculation platform). For graphene, we performed calculations using a 3 × 5 × 1 supercell (60 atoms). We used 2 × 2 × 2 k-point grids and a 60 R_y energy cutoff for the wave function, which ensured electronic and ionic convergence. The convergence criteria of the structural relaxation and electronic self-consistency for energy and forces set were chosen as 10⁻⁸ R_y and 0.000038 R_y/Bohr, respectively. In this setup, the calculated C–C bond length was 0.142 nm, which is in excellent agreement with the experimental value of 0.142 nm [53]. The calculated angle between the nearest neighboring atoms is 120°. For the bulk orthorhombic perovskite of ZTO, we used 6 × 6 × 4 k-point grids and a 50 R_y energy cutoff for the wave function, which ensured electronic and ionic convergence. The convergence criteria of the structural relaxation and electronic self-consistency for energy and forces set were chosen as 10⁻⁸ R_y and 0.000038 R_y/Bohr, respectively. In this setup, the calculated lattice parameters of a, b, and c were 0.5357 nm, 0.5363 nm, and 0.7919 nm, respectively, which is in close agreement with the other calculated values of 0.5381 nm, 0.5408 nm, and 0.7940 nm, respectively. To determine the formation energies for the substitution or absorption of Sn, Zn, O, SnO₃, and ZTO molecules on graphene, the slabs had a 15 Å-thick vacuum layer placed within the periodic cells repeated in the z-axis to obviate interactions. We used a 2 × 2 × 1 k-points mesh and a 60 R_y energy cutoff for the wave function. The van der Waals interactions were considered using the DFT-D3(BJ) method. All calculations were spin-polarized. The convergence criteria of the structural relaxation and electronic self-consistency for energy and forces set were chosen as 10⁻⁷ R_y and 0.00038 R_y/Bohr, respectively. To obtain the electronic transport properties of graphene bonded with ZTO molecules, we performed the QE and Boltzmann transport equation code, such as BoltzTrap [54].

2.3. Integration of ZTO-SMC into PDMS film and TENG

The PDMS elastomer and cross-linker (Sylgard 184, Dow Corning) were mixed at a weight ratio of 10:1. To prepare the PDMS-based triboelectric layer with ZTO-SMC, ZTO-SMC dispersed in toluene was first mixed with PDMS through mechanical stirring for 30 min and degassed under vacuum for approximately 1 h. The prepared mixture was poured into a Petri dish and stored in an oven at 160 °C for 1 h until it was cured. Finally, the cured PDMS-based triboelectric layer with ZTO-SMC (thickness of 500 μm) was peeled off from the Petri dish. To prepare the contact-separation-mode TENG, 2 × 2 cm² aluminum foil was fixed on two acrylic plates adhered with double-sided tape and an electrode made from copper wire. The triboelectric layer (2 × 2 cm²) was attached to the aluminum foil of the bottom acrylic plate and the top and bottom acrylic plates were fixed using four springs. The ZTO-SMC TENG (0.3 wt%) sample was plasma-treated at an RF power of 100 W with CF₄ and O₂ gases. Details of the RF plasma treatment conditions can be found in our previous study [52].

2.4. Electrical measurement and characterization

The harvesting devices were made for the test of repetitive contact and separation mode of triboelectric energy harvesting with a distance of 2 mm between two layers. Contact and separation modes for triboelectric energy harvesting were tested at a working frequency of 2 Hz and a force of 50 N. A Keithley preamplifier (model 6514) and an oscilloscope (Tektronix MDO3024) were utilized to perform electrical measurements. The morphology of the samples was analyzed through

field-emission SEM (FEI, Quanta FEG 250), 3D confocal interferometric microscopy (Leica, Leica DCM-8), and EDS or Cs-TEM (JEM-ARM200F, JEOL Ltd). Relative permittivity measurements of the triboelectric layer were performed using an impedance analyzer (HIOKI, IM 3570). Crystallographic information of all samples was acquired using an X-ray diffractometer (X-Pert Pro MPD, Malvern Panalytical) with Cu-K α radiation ($\lambda = 0.15418$ nm) at 40 kV and 100 mA. The binding energies of the elements in the samples were determined by XPS (PHI 5000 Versa Probe, Physical Electronics).

3. Results and discussion

Fig. 1a shows the schematic of the formation of ZTO-SMC via the PLA process. During the PLA process, high pressure and high temperature are generated around the adjacent area of the laser-irradiated surface. Thus, the PLA process causes physicochemical changes in the intrinsic properties of materials, including chemical composition, morphology, and crystal structure [55–58]. Fig. 1a(i) depicts that Zn²⁺ and Sn⁴⁺ ions and CNTs are dispersed in ethanol. When a mixed solution was irradiated with a pulsed laser, the outer wall of the CNTs collapses and ethanol (C₂H₅OH) decomposes. Subsequently, the oxygen functional groups (e. g., hydroxyl and carboxyl) on the surface of the CNTs are formed [59, 60]. Zn²⁺ and Sn⁴⁺ ions in the ethanol solvent combine with the collapsed CNT surface to form ZTO for minimizing the surface energy of the CNTs, as shown in Fig. 1a(ii) and 1a(iii). Spherical aberration-corrected transmission electron microscopy (Cs-TEM) and energy-dispersive X-ray spectroscopy (EDS) was performed to

investigate the structure and composition of the prepared ZTO-SMC; the results are shown in Fig. 1b–g. The injected pulsed laser collapses the surface of the CNTs (Fig. 1b and c). Subsequently, the formation of the ZTO occurs on the collapsed layer of the CNTs during the PLA process. (Fig. 1d and e). ZTO appears to be bound to CNTs without any voids and structural defects; the observed lattice fringe is 0.26 nm, corresponding to (111) of ZTO, as shown in Fig. 1f. The homogeneous elemental distribution of Zn, Sn, and O in ZTO and C on the SMCs was confirmed by elemental mapping analysis as shown in Fig. 1g.

Crystallographic information and chemical composition of the ZTO-SMC prepared by the PLA process were confirmed through X-ray diffractometry (XRD) and X-ray photoelectron spectroscopy (XPS). Fig. S1a presents the XRD patterns of ZTO-SMC, SMCs, and CNTs. The XPS results reveal the difference between CNTs and SMCs (presence of oxygen functional groups) and the formation of ZTO and oxygen functional groups (Zn–O, Sn–O, C=O, C–OH, and HO–C=O) in ZTO-SMCs prepared by PLA (Figs. S1b–h). These results indicate that the PLA process leads to the surface modification of the CNTs and crystallization of the ZTO. Additionally, Fig. S1i confirms the distribution of ZTO on the surface of the SMCs. Although many studies provide similar empirical descriptions of the pulsed laser ablation process for the crystallization of oxides, the mechanisms of the nucleation and subsequent formation or growth of the oxides on the SMC are not well understood from a fundamental standpoint. To better understand the formation of the ZTO-SMC, theoretical DFT calculation was carried out to determine the adsorption energy, binding energy, and quantitative adsorption energies of the Zn, Sn, O, and SnO₃ on graphene are given in Table S1. For the

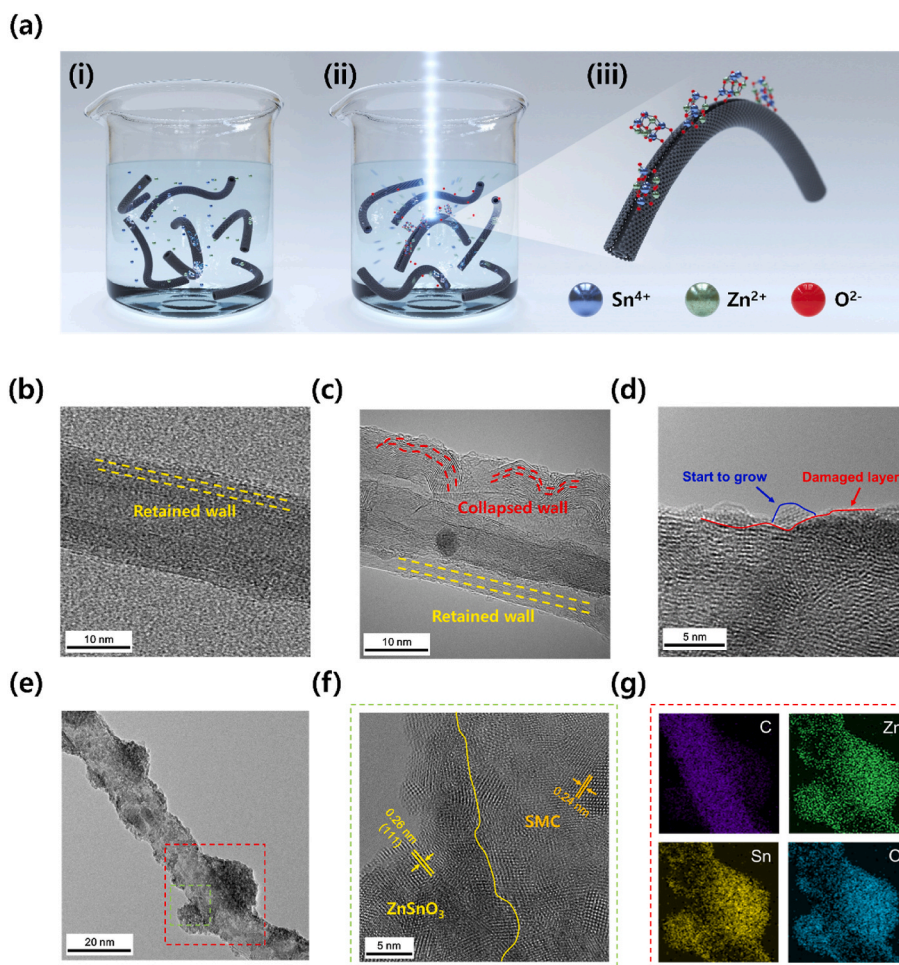


Fig. 1. (a) Schematic of the formation of ZTO-SMC, (b–f) HR-TEM and Cs-TEM images of the CNTs, the SMCs, and ZTO-SMC, and (g) element mapping profile of C, O, Zn, Sn of ZTO-SMC. (A colour version of this figure can be viewed online.)

calculation, the models considering the adsorption of several molecules and high index surfaces of ZTO on graphene were built as shown in Fig. S2 and Fig. 2. As illustrated in Fig. S2, it is evident that adsorption and bonding of O atoms to C atoms of graphene are more stable than those of Zn and Sn atoms. This implies that C atoms on the surface of CNT prefer to bond with O atoms during the initial stage for the formation of the ZTO. Also, the binding energies of various molecules in Fig. 2 clearly show that the SnO_3 structure is only stable when adsorbed and bonded with C atoms of graphene among the molecules. It is noted that the formation of perovskite structures such as ZTO is more stable than maintaining dissociated ionic states of Zn^{2+} and SnO_3^{2-} (Fig. S3). Hence, it is suggested that thermal energy generated by irradiation of a pulsed laser can promote the chemical bonding between C atoms of the SMCs and SnO_3^{2-} ions via pre-adsorption of O^{2-} ions. Subsequently, nucleation and growth of the ZTO occur through additional chemical reactions with Zn^{2+} ions in liquid medium containing precursors. From this result, it is expected that charge transfer between ZTO and SMC can be promoted to provide more surface charge density on the triboelectric layer. Experimental results from TEM, XRD, and XPS also support the clear evidence for the formation mechanism of the ZTO-SMC derived from DFT calculation.

TENG structure in this study simply consists of one triboelectric layer for triboelectrification and two Al electrodes for transferring electrical energy, which does not contain the triboelectric layer to demonstrate the role of a single ZTO-SMC added triboelectric layer on the performance of TENG. The structure of the prepared TENG is schematically presented in Fig. S4a. Basic working mechanism of the TENG is that electron flow is driven back and forth through the external circuit in the contact-separation process of the TENG, generating alternative current and voltage pulse [61]. In contact mode, when the PDMS triboelectric layer with ZTO-SMC fillers is getting closer to the Al electrodes on top by pressing, a potential difference is formed between two layers which drives the charge transfer between two electrodes (Figs. S4b and c) until the electrostatic balance is formed (Fig. S4d). Noted that the difference of charge affinity leads to the surface potential of the PDMS layer and top electrodes as negative and positive, respectively. In separation mode, when the bottom layer containing PDMS triboelectric layer is gradually away from the top electrode, charges move in the reverse direction due to decreased potential difference (Fig. 4Se). Such repeated

contact-separation processing provides alternating current signals to external loads [62,63].

The PDMS-based triboelectric layers containing different additives (pristine PDMS (P-PDMS), SMCs (0.05 wt%), and ZTO-SMC (0.05 wt%)) were prepared for evaluating TENG performance. It is clearly shown that the output performance of the TENG is gradually enhanced by the triboelectric layer with additives in the order of P-PDMS, SMCs, and ZTO-SMC. Especially, TENG containing ZTO-SMC exhibited an output voltage and a current density of 421.25 V and 77.33 mA m^{-2} , respectively (Fig. 3a and b). Enhanced triboelectric performance of the TENG (ZTO-SMC) can be explained by the coupling of the improved triboelectric effect and electrostatic induction. Repetitive contact and separation on the TENG result in the deformation of PDMS combined with the simultaneous alignment of the dipoles inside ZTO-SMC providing enhanced output performance between the top and bottom electrodes [61]. Also, considering the contact-separation mode of the TENG, the V-Q-x relationship of the TENG is given as follows [64]:

$$V = -\frac{Q}{S \cdot \epsilon_0} \left(\frac{d_{\text{PDMS}}}{\epsilon_r} + x(t) \right) + \frac{\sigma \cdot x(t)}{\epsilon_0} \quad (1)$$

where V represents the output voltage, Q indicates the amount of transfer charge between the two Al electrodes, and S denotes the effective friction area. ϵ_0 symbolizes the vacuum dielectric constant. Also, ϵ_r and d_{PDMS} represent the relative dielectric constant and thickness of the triboelectric layer, respectively. $x(t)$ represents the distance between Al electrodes and the triboelectric layer, and σ is the surface charge density of the triboelectric layer. Equation (1) indicates that the output voltage increases with the relative dielectric constant (ϵ_r) as well as surface charge density (σ) proportional to the capacitance, and thus the capacitance (C) of the device is given as follows [36,65]:

$$C = \frac{\epsilon_r \cdot S}{d_{\text{PDMS}} \cdot x(t)} \quad (2)$$

where the C is affected by the ϵ_r due to the similar thickness of the triboelectric layer in this study. Therefore, surface charge density and output voltage depend on the frictional area and dielectric constant. Also, the dielectric constant of the ZTO-SMC-embedded PDMS layer is increased. Based on the results, increased surface charge density

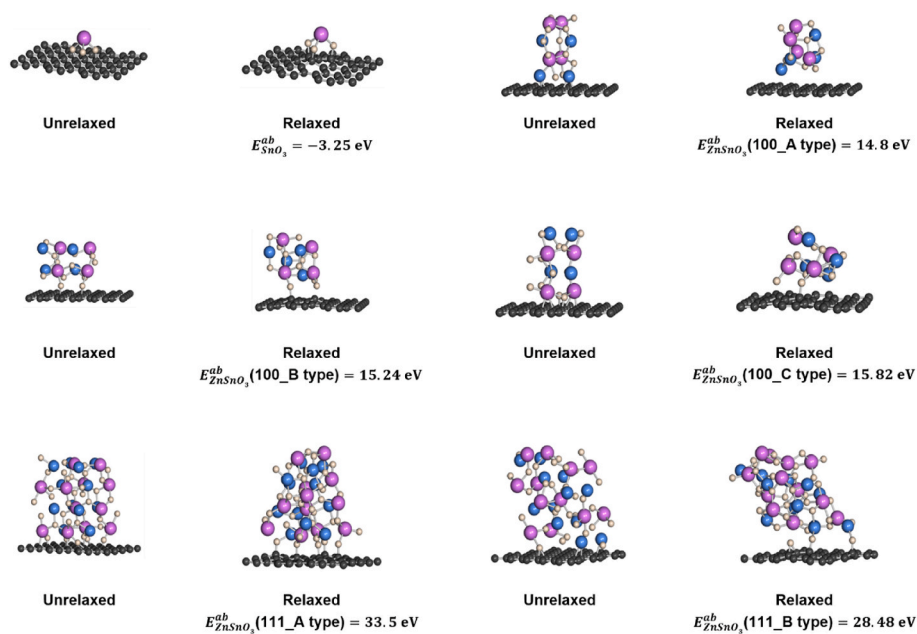


Fig. 2. Schematic of molecules models used in DFT calculations, and their absorbed energies required to stabilize the molecules (cream: O, blue: Zn, and purple: Sn). (A colour version of this figure can be viewed online.)

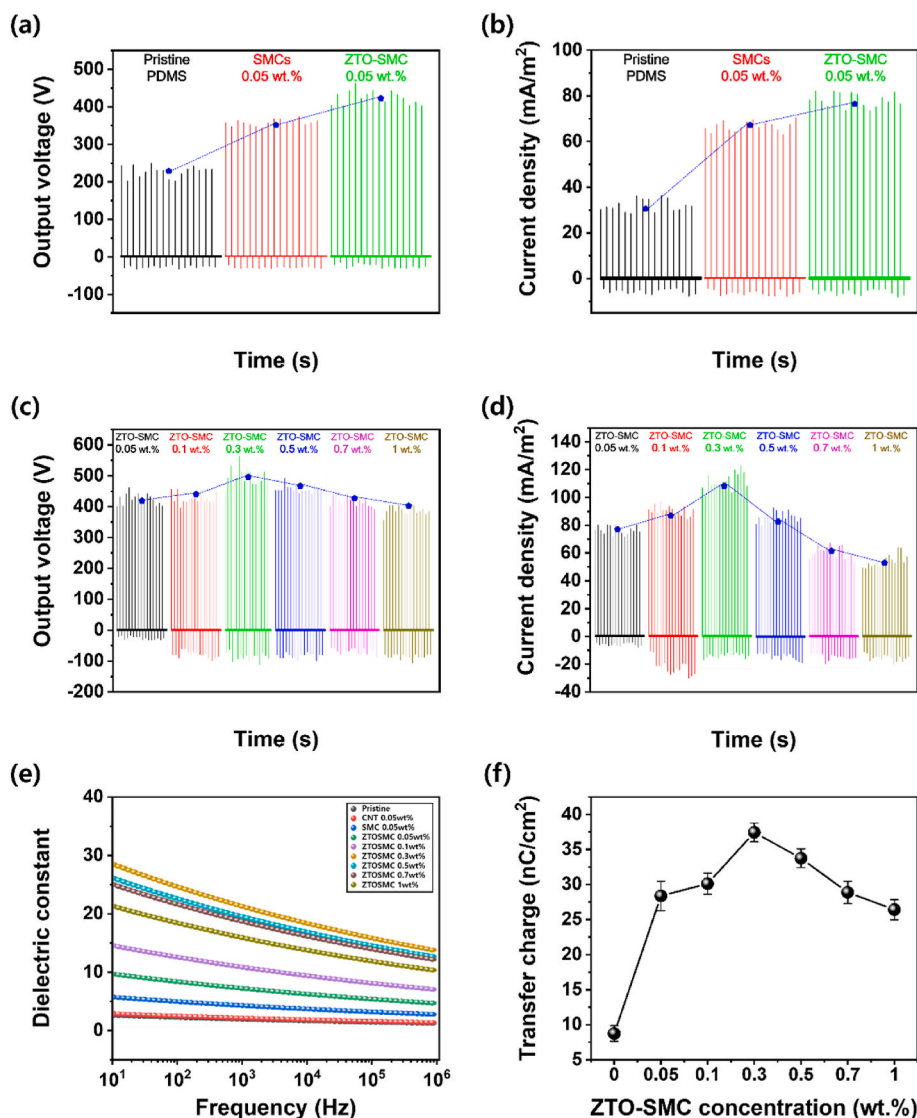


Fig. 3. (a) Output voltage and (b) current density of the PDMS-based TENGs with different type of additives under repetitive contact-separation mode. (c) Output voltage and (d) current density of TENGs using the PDMS-based triboelectric layer with ZTO-SMC concentrations under repetitive contact-separation mode. (e) Dielectric constant of the different triboelectric layers in the frequency between 10 and 10^6 . (f) Transfer charge of the triboelectric layer with different ZTO-SMC concentration from 0 wt% to 1 wt%. (A colour version of this figure can be viewed online.)

significantly results in the enhanced output performance of the TENG device. Combined with pressure-induced polarization alignment, the dielectric constant of the triboelectric layer can be another factor to achieve enhanced triboelectric performance.

We investigated the optimal concentration of ZTO-SMC in the PDMS-based layer to further enhance the TENG performance as presented in Fig. 3c and d. Cross-sectional micrographs of the ZTO-SMC added triboelectric layer show homogeneous distribution of ZTO-SMC within the PDMS matrix regardless of different concentrations (Fig. S5). As increasing the concentration of ZTO-SMC from 0.05 to 0.3 wt%, output voltage, and current density increased from 421.25 to 498.13 V and 77.33–108.43 mA m^{-2} , respectively. However, TENG output performance decreased when the concentration of the ZTO-SMC exceeded 0.3 wt%. The dielectric constant of the PDMS-based triboelectric layer with different ZTO-SMC concentrations was evaluated as shown in Fig. 3e. Similar to the results of output performance of the TENG containing the ZTO-SMC with different concentrations, the dielectric constant of the triboelectric layer is gradually increased with increased ZTO-SMC concentration. Also, the dielectric constant of the ZTO-SMC-added triboelectric layer exhibited a larger value than that of P-PDMS and CNTs or SMCs-added PDMS. However, excessive concentration of the conductive and/or dielectric fillers can result in the reduced output performance of the TENG [35–37]. Similarly, the dielectric constant of the PDMS-based

triboelectric layer with ZTO-SMC concentration is decreased when exceeded percolation threshold (>0.3 wt%), which makes the triboelectric layer conductive and reduces the effective frictional area, thereby reducing the surface charge density to directly deteriorate the output performance of the TENG. As expected, charge transfer is gradually decreased when exceeded the percolation threshold, which can be related to reduced surface charge density (Fig. 3f). Similar results of the TENG performance and dielectric constant depending on the ZTO-SMC concentration as shown in Fig. 3c and d.

Triboelectric charge transfer with the co-additives can be considered one of the important factors to affect the output performance of the PDMS-based TENG. To better understand the effect of ZTO-SMC on the charge transfer of PDMS-based TENG, DFT calculation was used to investigate the conduction behavior of ZTO-SMC [30,31]. The model structures investigated are graphene, and different types of perovskite ZTO on the graphene such as 100_A type, 100_B type, 111_A type, and 111_B type, illustrated in Fig. 2. It is noted that Density of states (DOS), and electrical conductivity along x- and y-axis of the graphene and different types of the ZTO on the graphene are shown in Fig. 4. The results indicate that all simulated models show decreased electrical conductivity at the fermi level. However, both 100_B type and 111_A type of the ZTO on graphene show a relatively smaller drop in electrical conductivity than that of graphene, which implies that unique ZTO-SMC

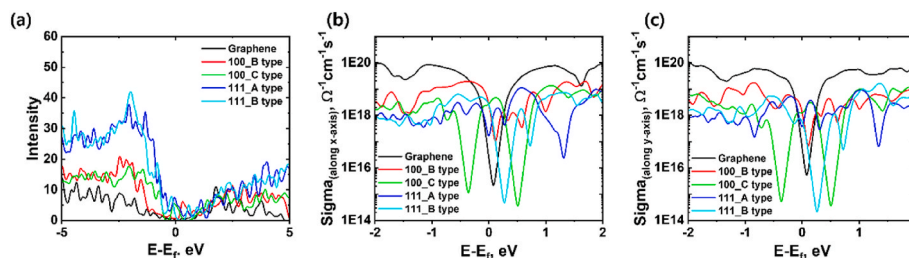


Fig. 4. (a) Density of states and (b, c) electrical conductivities of pure graphene and ZTO molecules on the graphene. (A colour version of this figure can be viewed online.)

heterostructure can promote charge transfer, compared to pure CNT. Also, a higher work function of the CNTs (5.6 eV) than that of ZTO (4.7 eV) creates a potential barrier between ZTO and CNTs, thus promoting more charge transfer to PDMS (Fig. S6) [66]. Experimental results combined with DFT calculation suggest that ZTO-SMC, which shows large dielectric constant, press-induced polarization, and related surface charge density, are suitable co-additive to enhance the performance of the PDMS-based TENG.

Radio frequency (RF) plasma treatment in CF_4 and O_2 gases was performed to further enhance the TENG performance, which aims at improving the effective frictional area of the device through the fluorination on the surface of the PDMS-based triboelectric layer [15,67]. Fig. S7 depicts the surface morphology of PDMS before and after the plasma treatment. Confocal microscopy images reveal that the surface of the PDMS layer after plasma treatment for 7 min becomes rougher. More details relating to the effect of the plasma treatment on the fluorination on the surface of the PDMS-based layer were found in our previous study [52]. As presented in Fig. 5a, the plasma treatment provides increased output voltage (665.63 V) and current (137.08 mA m^{-2}) of ZTO-SMC TENG, which is 2.95 and 4.53 times higher value compared to those of the P-PDMS TENG. Output performance of the ZTO-SMC TENG on load resistance was also investigated as shown in Fig. 5b and c. The instantaneous peak power density was calculated using equation (3) as follows:

$$P = \frac{I^2 \cdot R}{A} \quad (3)$$

where here A indicates the effective friction area of the TENG ($20 \times 20 \text{ mm}^2$). The results show that the peak power density increases up to 10.59 W m^{-2} at a load resistance of $7 \text{ M}\Omega$. Peak densities of the pristine PDMS TENG and SMC PDMS TENG at $10 \text{ M}\Omega$ were observed to be 2.4 W m^{-2} and 7.69 W m^{-2} , respectively. Quantitative results of the output voltage, output current density, and peak power density per unit area are summarized in Table S2, which indicates that the ZTO-SMC TENG exhibits the highest output performance, compared to that of other TENGs. Furthermore, the ZTO-SMC TENG exhibits excellent durability and stability without any obvious change in the output voltage as presented in Fig. 6 and b illustrates that the ZTO-SMC TENG can charge the capacitors of $0.15 \mu\text{F}$ quickly to a maximum voltage of 0.95 V within 1 s , providing the electric charge of 142.5 nC . The charging behaviour of the

various capacitors through operating the ZTO-SMC TENG is also presented in Fig. 6c. In the aspect of the energy harvesting, the output power from the ZTO-SMC TENG can light the 59 LED lamp beads to clearly show characters “KITECH” in Fig. 6d and can successfully power 488 commercial LED beads connected in series (Video S1, Supporting information).

4. Conclusions

We proposed the materials strategies to enhance the triboelectric performance of the PDMS-based TENG for effective energy harvesting using experimental and computational methods. Based on the DFT calculation, the formation mechanism of the ZTO-SMC as co-additive is elucidated: thermal energy generated by irradiation of pulsed laser can promote the bonding between C atoms of the SMCs and SnO_3^{2-} ions via adsorption of O^{2-} ions, and subsequent nucleation and growth of the ZTO occur through an additional chemical reaction with Zn^{2+} ions in liquid medium containing precursors. With applying effective co-additive and single-step fluorocarbon and O_2 gas plasma treatment, experimental results show that optimized ZTO-SMC TENG shows the highest output voltage (665.63 V), current (137.08 mA m^{-2}), and power density (10.57 W m^{-2}), which can be used as a sufficient power source not only to light up 59 commercial LED lamp beads connected in series but also to charge different types of capacitors. We conclude that the synergetic effect of the enhanced dielectric properties and effective frictional area improves the output performance of the ZTO-SMC TENG. This work opens an avenue for the rational design and fabrication of various co-additive for PDMS-based TENGs with enhanced triboelectric performance.

CRediT authorship contribution statement

Kangpyo Lee: Conceptualization, Investigation, Writing – original draft. **HyukSu Han:** Formal analysis, Writing – original draft. **Jeong Ho Ryu:** Data curation, Visualization. **Sukhyun Kang:** Investigation. **Kyunghwan Jung:** Validation. **Young-Kwang Kim:** Software. **Taeseup Song:** Validation. **Sungwook Mhin:** Project administration, Writing – review & editing. **Kang Min Kim:** Conceptualization, Supervision, All authors commented on the manuscript.

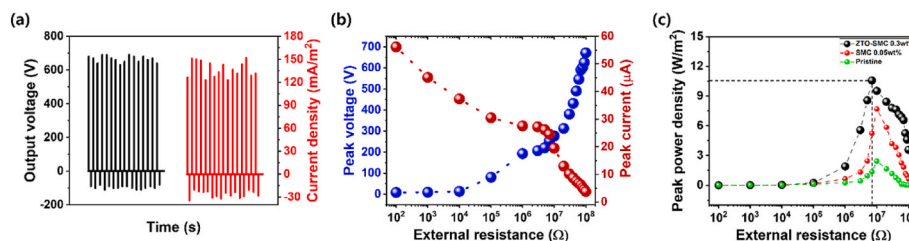


Fig. 5. (a) Output voltage and current density of the ZTO-SMC PDMS-based TENG under repetitive contact-separation mode. (b, c) Peak voltage, peak current, and peak power density under different external resistances. (A colour version of this figure can be viewed online.)

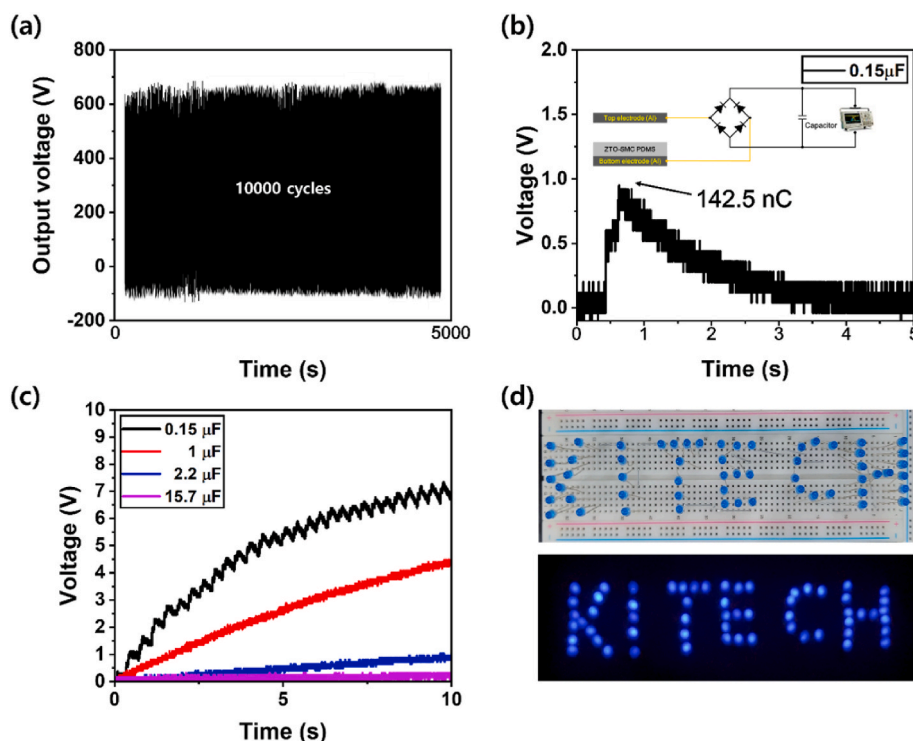


Fig. 6. (a) Output voltage of the ZTO-SMC-PDMS-based TENG under repetitive contact-separation mode (10000 cycles). (b) Charging the $0.15 \mu\text{F}$ capacitors through ZTO-SMC PDMS TENG under single contact-separation mode. (c) Charging of the capacitors with different capacity (0.15 , 1 , 2.2 , and $15.7 \mu\text{F}$). (d) 59 LED lamp beads connected in series, powered by ZTO-SMC-PDMS-based TENG. (A colour version of this figure can be viewed online.)

Declaration of competing interest

The authors declare that they have no known competing financial interests or personal relationships that could have appeared to influence the work reported in this paper.

Acknowledgements

This research was supported by the Basic Science Research Program through the National Research Foundation of Korea (NRF) funded by the Korea government (MSIT) (No. 2022R1A2C2008406, No. 2022R1A2C2010162 and 2023R1A2C1004549).

Appendix A. Supplementary data

Supplementary data to this article can be found online at <https://doi.org/10.1016/j.carbon.2023.118120>.

References

- [1] K.R. Singh, V. Nayak, J. Singh, R.P. Singh, Nano-enabled wearable sensors for the Internet of things (IoT), *Mater. Lett.* 304 (2021), 130614.
- [2] D. Verma, K.R. Singh, A.K. Yadav, V. Nayak, J. Singh, P.R. Solanki, R.P. Singh, Internet of things (IoT) in nano-integrated wearable biosensor devices for healthcare applications, *Biosens. Bioelectron.* X 11 (2022), 100153.
- [3] F.R. Fan, Z.Q. Tian, Z.L. Wang, Flexible triboelectric generator, *Nano Energy* 1 (2012) 328–334.
- [4] Z.L. Wang, On Maxwell's displacement current for energy and sensors: the origin of nanogenerators, *Mater. Today* 20 (2017) 74–82.
- [5] A. Khan, M.A. Abbasi, M. Hussain, Z.H. Ibupoto, J. Wissting, O. Nur, M. Willander, Piezoelectric nanogenerator based on zinc oxide nanorods grown on textile cotton fabric, *Appl. Phys. Lett.* 101 (2012), 193506.
- [6] Z.L. Wang, Triboelectric nanogenerators as new energy technology for self-powered systems and as active mechanical and chemical sensors, *ACS Nano* 7 (2013) 9533–9557.
- [7] M. Kim, Y. Ra, S. Cho, S. Jang, D. Kam, Y. Yun, H. Kim, D. Choi, Geometric gradient assisted control of the triboelectric effect in a smart brake system for self-powered mechanical abrasion monitoring, *Nano Energy* 89 (2021), 106448.
- [8] S. Zhang, J. Xu, J. Yu, L. Song, J. He, N. Ma, X. Hou, X. Chou, An all-rubber-based woven nanogenerator with improved triboelectric effect for highly efficient energy harvesting, *Mater. Lett.* 287 (2021), 129271.
- [9] S.D. Mahapatra, P.C. Mohapatra, A.I. Aria, G. Christie, Y.K. Mishra, S. Hofmann, V. K. Thakur, Piezoelectric materials for energy harvesting and sensing applications: roadmap for future smart materials, *Adv. Sci.* 8 (2021), 2100864.
- [10] H. Kuang, Y. Li, S. Huang, L. Shi, Z. Zhou, C. Gao, X. Zeng, R. Pandey, X. Wang, S. Dong, X. Chen, J. Yang, H. Yang, J. Luo, Piezoelectric boron nitride nanosheets for high performance energy harvesting devices, *Nano Energy* 80 (2021), 105561.
- [11] R.A. Surmenev, R.V. Chernozem, I.O. Pariy, M.A. Surmeneva, A review on piezo- and pyroelectric responses of flexible nano- and micropatterned polymer surfaces for biomedical sensing and energy harvesting applications, *Nano Energy* 79 (2021), 105442.
- [12] C. Yu, J. Park, J.R. Youn, Y.S. Song, Integration of form-stable phase change material into pyroelectric energy harvesting system, *Appl. Energy* 307 (2022), 118212.
- [13] R. Li, X. Wei, Y. Shi, Z. Yuan, B. Wang, J. Xu, L. Wang, Z. Wu, Z.L. Wang, Low-grade heat energy harvesting system based on the shape memory effect and hybrid triboelectric-electromagnetic nanogenerator, *Nano Energy* 96 (2022), 107106.
- [14] G. Miao, S. Fang, S. Wang, S. Zhou, A low-frequency rotational electromagnetic energy harvester using a magnetic plucking mechanism, *Appl. Energy* 305 (2022), 117838.
- [15] X. Cheng, B. Meng, X. Chen, M. Han, H. Chen, Z. Su, M. Shi, H. Zhang, Single-step fluorocarbon plasma treatment-induced wrinkle structure for high-performance triboelectric nanogenerator, *Small* 12 (2016) 229–236.
- [16] U. Khan, S.W. Kim, Triboelectric nanogenerators for blue energy harvesting, *ACS Nano* 10 (2016) 6429–6432.
- [17] J. Chen, J. Yang, Z. Li, X. Fan, Y. Zi, Q. Jing, H. Guo, Z. Wen, K.C. Pradel, S. Niu, Z. L. Wang, Networks of triboelectric nanogenerators for harvesting water wave energy: a potential approach toward blue energy, *ACS Nano* 9 (2015) 3324–3331.
- [18] X.S. Zhang, M. Su, J. Brugger, B. Kim, Penciling a triboelectric nanogenerator on paper for autonomous power MEMS applications, *Nano Energy* 33 (2017) 393–401.
- [19] F.R. Fan, L. Lin, G. Zhu, W. Wu, R. Zhang, Z.L. Wang, Transparent triboelectric nanogenerators and self-powered pressure sensors based on micropatterned plastic films, *Nano Lett.* 12 (2012) 3109–3114.
- [20] X.S. Zhang, M.D. Han, B. Meng, H.X. Zhang, High performance triboelectric nanogenerators based on large-scale mass-fabrication technologies, *Nano Energy* 11 (2015) 304–322.
- [21] H. Wu, W. He, C. Shan, Z. Wang, S. Fu, Q. Tang, H. Guo, Y. Du, W. Liu, C. Hu, Achieving remarkable charge density via self-polarization of polar high-k material in a charge-excitation triboelectric nanogenerator, *Adv. Mater.* 34 (2022), 2109918.
- [22] S. Liu, Y. Liu, Y. Chen, S. Wang, C. Men, S. Gao, Novel 3D printed vortex-like flexible roller-compacted triboelectric nanogenerator for self-powered

- electrochemical degradation of organic contaminants, *ACS Appl. Mater. Interfaces* 14 (2022) 17426–17433.
- [23] S. Gao, Y. Zhu, Y. Chen, M. Tian, Y. Yang, T. Jiang, Z.L. Wang, Self-power electroreduction of N_2 into NH_3 by 3D printed triboelectric nanogenerators, *Mater. Today* 28 (2019) 17–24.
- [24] C. Men, X. Liu, Y. Chen, S. Liu, S. Wang, S. Gao, Cotton-assisted dual rotor-stator triboelectric nanogenerator for real-time monitoring of crop growth environment, *Nano Energy* 101 (2022), 107578.
- [25] W. Chen, W. Wang, S. Li, J. Kang, Y. Zhang, Q. Yan, T. Guo, X. Zhou, C. Wu, Self-powered liquid crystal lens based on a triboelectric nanogenerator, *Nano Energy* 107 (2023), 108143.
- [26] H. Zou, Y. Zhang, L. Guo, P. Wang, X. He, G. Dai, H. Zheng, C. Chen, A.C. Wang, C. Xu, Z.L. Wang, Quantifying the triboelectric series, *Nat. Commun.* 10 (2019) 1427.
- [27] K.E. Byun, Y. Cho, M. Seol, S. Kim, S.W. Kim, H.J. Shin, S. Park, S.W. Hwang, Control of triboelectricity by engineering surface dipole and surface electronic state, *ACS Appl. Mater. Interfaces* 8 (2016) 18519–18525.
- [28] L. Xu, T.Z. Bu, X.D. Yang, C. Zhang, Z.L. Wang, Ultrahigh charge density realized by charge pumping at ambient conditions for triboelectric nanogenerators, *Nano Energy* 49 (2018) 625–633.
- [29] C. Wu, T.W. Kim, H.Y. Choi, Reduced graphene-oxide acting as electron-trapping sites in the friction layer for giant triboelectric enhancement, *Nano Energy* 32 (2017) 542–550.
- [30] H. Sun, H. Tian, Y. Yang, D. Xie, Y.C. Zhang, X. Liu, S. Ma, H.M. Zhao, T.L. Ren, A novel flexible nanogenerator made of ZnO nanoparticles and multiwall carbon nanotube, *Nanoscale* 5 (2013) 6117–6123.
- [31] X. Zhao, Z. Ounaies, A facile method to enhance the flexibility and triboelectric output of PDMS using ionic liquid-coated single-wall carbon nanotubes, *Nano Energy* 94 (2022), 106908.
- [32] S.M.S. Rana, M.T. Rahman, M. Salauddin, S. Sharma, P. Maharjan, T. Bhatta, H. Cho, C. Park, J.Y. Park, Electrospun PVDF-TrFE/MXene nanofiber mat-based triboelectric nanogenerator for smart home appliances, *ACS Appl. Mater. Interfaces* 13 (2021) 4955–4967.
- [33] Y. Zhu, B. Yang, J. Liu, X. Wang, L. Wang, X. Chen, C. Yang, A flexible and biocompatible triboelectric nanogenerator with tunable internal resistance for powering wearable devices, *Sci. Rep.* 6 (2016), 22233.
- [34] R. Zhang, C. Dahlström, H. Zou, J. Jonzon, M. Hummelgard, J. Örtengren, N. Blomquist, Y. Yang, H. Andersson, M. Olsen, M. Norgren, H. Olin, Z.L. Wang, Cellulose-based fully green triboelectric nanogenerators with output power density of 300 W m^{-2} , *Adv. Mater.* 32 (2020), 2002824.
- [35] P. Zhang, W. Zhang, L. Deng, H. Zhang, A triboelectric nanogenerator based on temperature-stable high dielectric $BaTiO_3$ -based ceramic powder for energy harvesting, *Nano Energy* 87 (2021), 106176.
- [36] J. Chen, H. Guo, X. He, G. Liu, Y. Xi, H. Shi, C. Hu, Enhancing performance of triboelectric nanogenerator by filling high dielectric nanoparticles into sponge PDMS film, *ACS Appl. Mater. Interfaces* 8 (2016) 736–744.
- [37] D. Park, S.H. Shin, L.J. Yoon, J. Nah, Ferroelectric nanoparticle-embedded sponge structure triboelectric generators, *Nanotechnol* 29 (2018), 185402.
- [38] N. Soin, P. Zhao, K. Prashanthi, J. Chen, P. Ding, E. Zhou, T. Shah, S.C. Ray, C. Tsonos, T. Thundat, E. Siores, J. Luo, High performance triboelectric nanogenerators based on phase-inversion piezoelectric membranes of poly(vinylidene fluoride)-zinc stannate (PVDF-ZnSnO₃) and polyamide-6 (PA6), *Nano Energy* 30 (2016) 470–480.
- [39] S. Kang, S.H. Kim, H.B. Lee, S. Mhin, J.H. Ryu, Y.W. Kim, J.L. Jones, Y. Son, N. K. Lee, K. Lee, Y. Kim, K.H. Jung, H. Han, S.H. Park, K.M. Kim, High-power energy harvesting and imperceptible pulse sensing through peapod-inspired hierarchically designed piezoelectric nanofibers, *Nano Energy* 99 (2022), 107386.
- [40] A. Sasmal, A. Patra, P.S. Devi, S. Sen, Space charge induced augmented dielectric permittivity and improved energy harvesting ability of nano-Ag decorated ZnSnO₃ filled PVDF based flexible nanogenerator, *Compos. Sci. Technol.* 213 (2021), 108916.
- [41] Q. Ye, Y. Wu, Y. Qi, L. Shi, S. Huang, L. Zhang, M. Li, W. Li, X. Zeng, H. Wo, X. Wang, S. Dong, S. Ramakrishna, J. Luo, Effects of liquid metal particles on performance of triboelectric nanogenerator with electrospun polyacrylonitrile fiber films, *Nano Energy* 61 (2019) 381–388.
- [42] L. Zhang, P. Bass, Z.Y. Cheng, Revisiting the percolation phenomena in dielectric composites with conducting fillers, *Appl. Phys. Lett.* 105 (2014), 042905.
- [43] X. Liu, P. Hu, J. Yu, M. Fan, X. Ji, B. Sun, Y. Shen, Topologically distributed one-dimensional TiO_2 nanofillers maximize the dielectric energy density in a PVDF-HFP nanocomposite, *J. Mater. Chem. A* 8 (2020) 18244–18253.
- [44] Z. Liu, K. Wang, X. Jiang, Overcoming current leaks in CNT/PDMS triboelectric composites by wrapping CNTs with TiO_2 insulation layer, *Appl. Phys. Lett.* 121 (2022), 113902.
- [45] S. Feng, H. Zhang, D. He, Y. Xu, A. Zhang, Y. Liu, J. Bai, Synergistic effects of $BaTiO_3$ /multiwall carbon nanotube as fillers on the electrical performance of triboelectric nanogenerator based on polydimethylsiloxane composite films, *Energy Technol* 7 (2019), 1900101.
- [46] K.I. Park, S.B. Bae, S.H. Yang, H.I. Lee, K. Lee, S.J. Lee, Lead-free $BaTiO_3$ nanowires-based flexible nanocomposite generator, *Nanoscale* 6 (2014) 8962–8968.
- [47] D. Tantraviwat, M. Ngamyngyoud, W. Sriprumkhai, P. Pattamang, G. Rujjanagul, B. Inceesungvorn, Tuning the dielectric constant and surface engineering of a $BaTiO_3$ /porous PDMS composite film for enhanced triboelectric nanogenerator output performance, *ACS Omega* 6 (2021) 29765–29773.
- [48] K.I. Park, M. Lee, Y. Liu, S. Moon, G.T. Hwang, G. Zhu, J.E. Kim, S.O. Kim, D. K. Kim, Z.L. Wang, K.J. Lee, Flexible nanocomposite generator made of $BaTiO_3$ nanoparticles and graphitic carbons, *Adv. Mater.* 24 (2012) 2999–3004.
- [49] S. Guan, Y. Tang, S. Song, H. Liu, S. Zhao, Influence of inter structure of $BaTiO_3$ -carbon nanotube hybrid particles on the dielectric properties of PDMS nanocomposites, *Mater. Sci. Eng. B* 271 (2021), 115280.
- [50] X. Xia, J. Chen, G. Liu, M.S. Javed, X. Wang, C. Hu, Aligning graphene sheets in PDMS for improving output performance of triboelectric nanogenerator, *Carbon* 111 (2017) 569–576.
- [51] Z. Kinas, A. Karabiber, A. Yar, A. Ozen, F. Ozel, M. Ersöz, A. Okbaz, High-performance Triboelectric Nanogenerator Based on Carbon Nanomaterials Functionalized Polyacrylonitrile Nanofibers, *Energy* 239 Part D, 2022, 122369.
- [52] K. Lee, S. Mhin, H. Han, O. Kwon, W.B. Kim, T. Song, S. Kang, K.M. Kim, A high-performance PDMS-based triboelectric nanogenerator fabricated using surface-modified carbon nanotubes via pulsed laser ablation, *J. Mater. Chem. A* 10 (2022) 1299–1308.
- [53] R. Heyrovska, Atomic Structures of Graphene, Benzene Methane with Bond Lengths as Sums of the Single, Double Resonance Bond Radii of Carbon, 2008.
- [54] G.K.H. Madsen, D.J. Singh, BoltzTraP. A code for calculating band-structure dependent quantities, *Comput. Phys. Commun.* 175 (2006) 67–71.
- [55] C.Y. Shih, M.V. Shugaev, C. Wu, L.V. Zhigilei, The effect of pulse duration on nanoparticle generation in pulsed laser ablation in liquids: insights from large-scale atomistic simulations, *PCCP* 22 (2020) 7077–7099.
- [56] D. Zhang, B. Gökce, S. Barcikowski, Laser synthesis and processing of colloids: fundamentals and applications, *Chem. Rev.* 117 (2017) 3990–4103.
- [57] J. Xiao, P. Liu, C.X. Wang, G.W. Yang, External field-assisted laser ablation in liquid: an efficient strategy for nanocrystal synthesis and nanostructure assembly, *Process Mater. Sci.* 87 (2017) 140–220.
- [58] P. Liu, H. Cui, C.X. Wang, G.W. Yang, From nanocrystal synthesis to functional nanostructure fabrication: laser ablation in liquid, *Phys. Chem. Chem. Phys.* 12 (2010) 3942–3952.
- [59] S. Kang, H. Han, S. Mhin, H.R. Chae, W.R. Kim, K.M. Kim, Ni-doped carbon nanotubes fabricated by pulsed laser ablation in liquid as efficient electrocatalysts for oxygen evolution reaction, *Appl. Surf. Sci.* 547 (2021), 149197.
- [60] S. Kang, K.H. Jung, S. Mhin, Y. Son, K. Lee, W.R. Kim, H. Choi, J.H. Ryu, H. Han, K. M. Kim, Fundamental understanding of the formation mechanism for graphene Quantum dots fabricated by pulsed laser fragmentation in liquid: experimental and theoretical insight, *Small* 16 (2020), 2003538.
- [61] G. wang, Y. Xi, H. Xuan, R. Liu, X. Chen, L. Cheng, Hybrid nanogenerators based on triboelectricification of a dielectric composite made of lead-free ZnSnO₃ nanocubes, *Nano Energy* 18 (2015) 28–36.
- [62] H. Wang, M. Shi, K. Zhu, Z. Su, X. Cheng, Y. Song, X. Chen, Z. Liao, M. Zhang, H. Zhang, High performance triboelectric nanogenerators with aligned carbon nanotubes, *Nanoscale* 8 (2016) 18489–18494.
- [63] W. Sun, Z. Jiang, X. Xu, Q. Han, F. Chu, Electromechanical coupling modeling and analysis of contact-separation mode triboelectric nanogenerators, *Int. J. Non Linear Mech.* 136 (2021), 103773.
- [64] S. Niu, S. Wang, L. Lin, Y. Liu, Y.S. Zhou, Y. Hu, Z.L. Wang, Theoretical study of contact-mode triboelectric nanogenerators as an effective power source, *Energy Environ. Sci.* 6 (2013) 3576–3583.
- [65] X. He, H. Guo, X. Yue, J. Gao, Y. Xi, C. Hu, Improving energy conversion efficiency for triboelectric nanogenerator with capacitor structure by maximizing surface charge density, *Nanoscale* 7 (2015) 1896–1903.
- [66] S.P. Kim, M.Y. Choi, H.C. Choi, Characterization and photocatalytic performance of SnO₂-CNT nanocomposites, *Appl. Surf. Sci.* 357 (2015) 302–308.
- [67] H. Kang, C. Zhao, J. Huang, D.H. Ho, Y.T. Megra, J.W. Suk, J. Sun, Z.L. Wang, Q. Sun, J.H. Cho, Fingerprint-Inspired conducting hierarchical wrinkles for energy-harvesting E-skin, *Adv. Funct. Mater.* 29 (2019), 1903580.